

1
2
3
4
5
6
7
8
9
10
11
12
13
14
15
16
17
18
19
20
21
22
23
24

Revised Manuscript (First Revision)

**Defect Contributions to the Heat Capacities and Stabilities of Some Chain,
Ring and Sheet Silicates, with Implications for Mantle Minerals**

H. Wayne Nesbitt¹, A.N. Cormack², Grant S. Henderson³

¹Dept. of Earth Sciences, Univ. of Western Ontario, London On., N6A 5B7, Canada

²New York State College of Ceramics, Alfred Univ., Alfred, NY 14802, USA

³Dept. of Earth Science, Univ. of Toronto, Toronto On., M5S 3B1, Canada

Corresponding Author:

H. Wayne Nesbitt, Tel: (519) 661-2100 ext. 83194, e-mail: hwn@uwo.ca

ABSTRACT

25
26 At temperatures less than $\sim 1500\text{K}$, previously published C_p data demonstrate that the heat
27 capacities of orthoenstatite, proto-enstatite, diopside and pseudowollastonite include primarily
28 Debye type vibrational and anharmonic contributions whereas the alkali chain, sheet and ring
29 silicates, Na_2SiO_3 , Li_2SiO_3 , K_2SiO_3 and $\text{Na}_2\text{Si}_2\text{O}_5$ include a third contribution. The third
30 contribution to C_p arises from defect formation due to the mobility Na, K, Li, and O^{2-} . The
31 contribution becomes apparent at temperatures above 700-800K for Na and K silicates, and above
32 900-1000K for Li metasilicate. With strong thermal agitation, alkali-non-bridging oxygen (NBO)
33 bonds are ruptured with the cations exiting their structural sites to occupy interstitial sites, thereby
34 producing intrinsic Frenkel defects which contribute to the C_p of the alkali silicates. The
35 magnitudes of the C_p defect contributions correlate inversely with cation-oxygen bond strengths, as
36 measured by bond dissociation energies. K-O and Na-O bond strengths are weak (239 and 257
37 kJ/mol) and defect contributions are large for these alkali chain, ring and sheet silicates. The
38 greater bond strength of Li-O (341 kJ/mol) correlates with a weaker defect contribution to the C_p
39 of Li_2SiO_3 . Mg-O and Ca-O bonds are stronger still (394 and 464 kJ/mol) and no C_p defect
40 contributions are observed for the pyroxenes and pseudowollastonite up to $\sim 1500\text{K}$.

41 Above $\sim 800\text{K}$ a polymerization reaction occurs in Na_2SiO_3 which produces some Q^3
42 species and free oxygen (O^{2-} or oxide ion). The polymerization reaction annihilates an oxygen
43 structural site so that the O^{2-} produced must reside on non-structural sites thus producing intrinsic
44 anionic defects. The same reactions likely occur in $\text{Na}_2\text{Si}_2\text{O}_5$ and K_2SiO_3 . Raman spectra of
45 Na_2SiO_3 indicate $>10\%$ of Na^+ and $\sim 1.7\%$ of O^{2-} on interstitial sites at 1348K.

46 Ca- and Mg-bearing mantle minerals subjected to temperature greater than $\sim 1500\text{K}$
47 experience the destabilizing effects of disordering (Frenkel defect formation). The minerals may

48 respond either by changing their composition or by changing phase. An abundance of Ca and Na
49 defects in pyroxenes, for example, likely promote production of new components (e.g., $\text{CaAl}_2\text{SiO}_6$,
50 $\text{NaAlSi}_2\text{O}_6$) in pyroxenes. By their production, Ca and Na defect concentrations are reduced
51 thereby stabilizing the phases. Mg-O bond dissociation and production of intrinsic Mg^{2+} and O^{2-}
52 point defects within olivine likely destabilize it and promote the phase transition to wadsleyite at
53 the base of the upper mantle.

54 **Keywords:** heat capacity of silicate minerals, Frenkel defects in silicates, Cation Disorder, Silicate
55 mineral stability, stability of mantle minerals

56

57

INTRODUCTION

58 Richet et al. (1996) compared the temperature dependence of the heat capacities (C_p) of the
59 isostructural chain silicates $\text{Li}_2\text{SiO}_3(\text{c})$ and $\text{Na}_2\text{SiO}_3(\text{c})$, and noted that C_p of $\text{Na}_2\text{SiO}_3(\text{c})$ was
60 consistently greater than that of $\text{Li}_2\text{SiO}_3(\text{c})$, regardless of temperature. The differing values below
61 $\sim 600\text{K}$ may be due to different Debye Temperatures (θ) of the phases because θ affects mostly the
62 low temperature C_p values of a phase. At higher temperatures, θ values have minimal effect on
63 heat capacity at constant volume (C_v), or on C_p , in that C_v approaches the universal value of $3nR$
64 regardless of θ values. Richet et al. (1996) explored these differences at both low and high
65 temperatures using sophisticated C_p models (e.g., Kieffer, 1982; 1980), which included
66 anharmonic effects, and they summarized the situation by stating that the excess C_p of Na_2SiO_3
67 remained unexplained. We address this conundrum by evaluating previously published
68 contributions to C_p of eight chain, ring and sheet silicates, orthoenstatite (MgSiO_3), proto-enstatite
69 (MgSiO_3), diopside ($\text{MgCaSi}_2\text{O}_6$), pseudowollastonite (CaSiO_3), Na_2SiO_3 , $\text{Na}_2\text{Si}_2\text{O}_5$, K_2SiO_3 and
70 Li_2SiO_3 . All crystals contain Q^2 species (silicate chains or rings) except $\text{Na}_2\text{Si}_2\text{O}_5$ which is a sheet
71 silicate consisting of Q^3 species (where Q represents a Si tetrahedron and the superscript indicates

72 the number of bridging oxygen atoms bonded to the central Si atom of the tetrahedron).

73 Cations of some crystals, heated to high temperature, may become mobile through rupture
74 of oxygen-cation bonds (e.g., Nesbitt et al., 2017; George et al., 1998) thereby contributing to
75 disorder by forming intrinsic defects (e.g., Frenkel defects). There is overwhelming evidence for
76 high temperature alkali and alkaline earth cation disorder in chain and ring silicates (Courtial et al.,
77 2000; Thiéblot et al., 1999; Richet et al., 1998, 1996, 1993; George et al., 1998; Dimanov and
78 Jaoul, 1998; Dimanov and Ingrin, 1995). George et al. (1998), for example, conducted a study of
79 Na_2SiO_3 and Li_2SiO_3 by collecting ^7Li , ^{23}Na and ^{29}Si NMR spectra as a function of temperature.
80 The study indicated limited Li mobility at high temperature. For Na_2SiO_3 , motional averaging
81 commenced at $\sim 700\text{-}800\text{K}$ and at $\sim 900\text{-}1000\text{K}$, Na^+ was sufficiently mobile to behave in a liquid-
82 like, disordered manner, residing on both structural and non-structural sites (George et al., 1998).
83 Recently, Nesbitt et al. (2017) emphasized that Na^+ and O^{2-} disorder occurred in Na_2SiO_3 crystals
84 at temperatures as low as $700\text{-}800\text{K}$, and well *before* the premelting region of the crystal was
85 encountered (Fig. 1a).

86 An appreciation for the problem to be addressed is gained by plotting C_p of Na_2SiO_3 against
87 temperature (Fig. 1a). Three sets of C_p data are plotted and they are reasonably consistent
88 (addressed subsequently). An obvious aspect is the rapid increase in C_p within the premelting
89 region (e.g., Richet et al., 1994) beginning at $\sim 1200\text{K}$. A less obvious aspect is the almost linear
90 increase in C_p between $\sim 400\text{K}$ and $\sim 1200\text{K}$, the slope of which is appreciably steeper than
91 expected considering that the rule of Dulong and Petit (Slater, 1963) requires the heat capacity to
92 reach a high temperature limit of $3nR$ ($\sim 149 \text{ J mol}^{-1}\text{K}^{-1}$ for Na_2SiO_3). To emphasize this aspect, C_p
93 of Na_2SiO_3 has been normalized to the number of atoms ‘n’ in the formula unit ($n=6$ for Na_2SiO_3)
94 to yield a “normalized C_p ” (i.e., C_p/n). The normalized experimental data are plotted against

95 temperature in Figure 1b as is the heat capacity (C_v) calculated using the Debye Function where
96 the Debye Temperature (θ) = 750K (Fig. 1b, dashed curve and Table 1). The Debye Function (i.e.,
97 C_v) reproduces reasonably well the normalized C_p data in the range 300K to 600K but C_v deviates
98 from experiment between ~700K and 1200K. It may result from anharmonic contributions to C_p
99 but Richet et al. (1996) concluded that C_v and anharmonic contributions alone cannot account for
100 the discrepancy. We address this discrepancy and attempt to explain it.

101 **THERMODYNAMICS ASPECTS**

102 Heat capacity includes at least two major contributions between ~300K and the premelting
103 region of a crystal. One is the heat capacity at constant volume (C_v or Debye Function) which
104 derives from the ‘Debye elastic continuum’ (Ghose et al., 1991; Keifer, 1980; Debye, 1912; Born
105 and von Kármán, 1912; Einstein, 1907). Anharmonic contributions constitute the second
106 contribution arising from the nature of site potentials within a crystal, which give rise to thermal
107 expansion. The two contributions allow calculation of C_p according to:

$$108 \quad C_p = C_v + [\alpha_v^2 V / \beta] T \quad (1)$$

109 where V is the volume of the phase, α_v is the volume coefficient of thermal expansion, β is the
110 compressibility and T is temperature. With V , α and β of a crystal known, the anharmonic term,
111 $[\alpha_v^2 V / \beta] T$, can be evaluated and C_p calculated as a function of temperature (provided C_v is
112 known). Equation (1) can be simplified using a relationship elucidated by Grüneisen (1912; 1926):

$$113 \quad \alpha_v V / \beta = \gamma C_v \quad (2)$$

114 where γ is the thermal Grüneisen parameter (Slater, 1963, p. 238). Substitution of Equation (2) into
115 Equation (1) and rearrangement yields:

$$116 \quad C_p = (1 + \alpha_v \gamma T) C_v \quad (3)$$

117 Estimates of the Grüneisen parameter for chain silicates range from 0.88 to 1.3 (Table 2; see also

118 Angel and Jackson, 2002) with the average value being 1.1 ($n = 7$, $\sigma = 0.15$). The average is used
119 in subsequent calculations. The γ parameter is largely independent of temperature (Slater, 1963, p.
120 219) and is similar for all silicates studied here (Angel and Jackson, 2002; Hofmeister and Mao,
121 2002; Ita and Stixrude, 1992; Jeanloz and Thompson, 1983).

122 The volume of crystalline Na_2SiO_3 is illustrated in Figure 2a where the solid circles
123 represent volumes from 298 to $\sim 1200\text{K}$ and the open circles represent measurements within the
124 premelting region. A linear least squares best fit to the solid circles was performed and the fit is
125 plotted on the figure. The slope, (dV/dT) is effectively constant at $\sim 1.43 \times 10^{-2}$ ($\text{\AA}^3/\text{K}$). The
126 coefficient of thermal expansion is defined as:

$$127 \quad \alpha_V = (dV/dT)_p/V \quad (4)$$

128 where 'p' denotes constant pressure. Because dV/dT is effectively constant, calculation of α_V
129 requires only that it be divided by V at the temperature of interest. The resulting α_V values for
130 Na_2SiO_3 are plotted on Figure 2b and α_V is effectively linear in T . The same procedure was used to
131 obtain α_V for other crystals studied and the results are illustrated in Figures 2c to 2f.

132 Accurate calculation of C_V for silicate crystals is complex (e.g., Ghose et al., 1991; Keiffer,
133 1982; 1980) but as noted in the Introduction, reasonable estimates of C_V can be obtained using the
134 Debye Function or a modification of it. The Debye Function (e.g, Table 1) employs only one
135 adjustable parameter, the Debye Temperature (θ), which can be evaluated from elastic or other
136 properties of the crystal (Grimvall, 2001). In the approach used here, the Debye Temperature is
137 treated as a fit parameter. To obtain approximate C_V values for a crystal, the Debye Temperature is
138 adjusted to provide a good fit to the heat capacity *in a specified temperature range* (here 300-600
139 K). The same θ value necessarily yields reasonable estimates of C_V at high temperature because the
140 Debye Function (C_V) approaches $3nR$ regardless of the value of θ . Treating θ as a fit parameter has

141 the advantage that the calculation of C_v may accommodate other moderate temperature lattice
142 contributions such as some optical modes (Ghose et al., 1991; Kieffer, 1980). Highly accurate
143 estimates of C_v are not required for this exercise, and the Debye Function is used to calculate C_v .

144 CALCULATED AND EXPERIMENTAL C_p DATA

145 Orthoenstatite and Proto-enstatite

146 Three sets of experimental C_p data are plotted on Figure 3a. The large open and shaded
147 circles represent, respectively, C_p of orthoenstatite and proto-enstatite. The values are derived from
148 relative enthalpies (heat contents) reported by Thiéblot et al. (1999). They measured the heat
149 evolved upon cooling a sample from a temperature T to a reference temperature ($T^* = 273$ K). The
150 heat evolved is the *difference* in enthalpy (H) at the two temperatures ($H_T - H_{T^*}$). A finite
151 difference approach was used to estimate an average C_p (i.e., $C_p(\text{av})$) over the temperature range of
152 any two measurements. Subtracting two heat content measurements (one at T_2 and one at T_1)
153 yields $(H_{T_2} - H_{T_1})$ and dividing it by the difference in the two temperatures ($T_2 - T_1$) gives $C_p(\text{av})$:

$$154 \quad C_p(\text{av}) = (H_{T_2} - H_{T_1}) / (T_2 - T_1) = \Delta H / \Delta T \quad (5)$$

155 The $C_p(\text{av})$ value represents the average C_p over the interval T_1 to T_2 and may be plotted on Fig. 3
156 at $T(\text{av}) = (T_2 - T_1) / 2$. T_1 need not be T^* and may be any temperature at which a heat content
157 measurement has been made. The original relative enthalpies of Thiéblot et al. (1999) for
158 orthoenstatite and proto-enstatite are reproduced in Table 3 and were used to calculate $C_p(\text{av})$,
159 which were, in turn, normalized to 'n' to obtain $C_p(\text{av})/n$ ($n=5$ for MgSiO_3). Heat capacities
160 derived from relative enthalpies commonly are of lower precision than those obtained by other
161 techniques due to subtraction of two large numbers. The resulting values are, however, devoid of
162 assumptions and propagation of errors, and may be more accurate than techniques which include
163 assumptions and propagation of errors. Use of $C_p(\text{av})$ to approximate C_p introduces minimal

164 uncertainty in C_p above about 700K, as now shown. The average value of T_2-T_1 of Table 3 is
165 $\sim 100\text{K}$ so that the temperature range associated with each $C_p(\text{av})$ is about $\pm 50\text{K}$. Uncertainty of
166 this magnitude does not affect the conclusions drawn subsequently.

167 The small circles of Figure 3a represent experimental $C_p(\text{av})/n$ values for a synthetic
168 orthoenstatite. The large open and shaded circles represent $C_p(\text{av})/n$ data for orthoenstatite and
169 proto-enstatite, respectively. The small and large circles merge between $\sim 450\text{K}$ and 800K ,
170 substantiating the accuracy of both sets of data. There is a group of measurements between 850K
171 and 1000K (Fig. 3a, small circles) which is offset to slightly greater C_p values relative to the other
172 data. These 'offset' data are not considered in the following discussion.

173 A Debye Temperature of 875K was used to calculate C_v for both enstatites and C_v is plotted
174 in Figure 3a as the dashed curve. The expression for α_v provided in Figure 2c and the Grüneisen
175 parameter ($=1.1$) were employed to calculate C_p according to Equation (3). The result is illustrated
176 by the solid curve of Figure 3a. The solid curve reproduces (within experimental uncertainty) the
177 orthoenstatite and proto-enstatite experimental values up to $\sim 1650\text{K}$ and the difference between the
178 solid curve and the dashed curve represents the anharmonic contribution to C_p . Clearly there are
179 only two major contributions to C_p of the enstatites between $\sim 300\text{K}$ and the premelting region of
180 proto-enstatite. Moreover, the α_v and Grüneisen parameter used in the calculations are reasonable
181 for both enstatites. Finally, the conformity of the calculated and experimental C_p values indicates
182 that the Debye Function provides reasonable estimates of C_v for the enstatites.

183 **Diopside**

184 Two sets of experimental C_p data for diopside ($\text{CaMgSi}_2\text{O}_6$) are plotted on Figure 3b and
185 they merge smoothly. With a Debye Temperature of 900K , the α_v expression of Figure 2b and a
186 Grüneisen parameter of 1.1 , the C_p values for diopside were calculated (Eq. 3) and plotted as the

187 solid curve of Figure 3b. The solid curve conforms closely to the experimental data up to ~1500K,
188 beyond which premelting and Ca disorder commences (Dimanov and Jaoul, 1998; Richet et al.,
189 1998; Dimanov and Ingrin, 1995; Richet et al., 1994; Richet and Fiquet, 1991). As for
190 orthoenstatite and proto-enstatite, there are two major contributions to the C_p of diopside, C_v and
191 an anharmonic contribution. Diopside is structurally different from the enstatite polymorphs but
192 the same Grüneisen parameter (1.1) allows reasonable estimates of C_p for the three crystals.

193 **Pseudowollastonite**

194 The C_p/n ($n=5$) values calculated for two sets of experimental data are plotted on Figure
195 3c. The C_v of pseudowollastonite (CaSiO_3) was calculated with $\theta = 900\text{K}$ and plotted on Figure 3c
196 (dashed curve). The expression for α_v (Fig. 2f) and a Grüneisen parameter = 1.1 were used to
197 calculate the effect of anharmonicity (Eq. 3) and the solid curve represents the result. The essential
198 agreement between experiment and calculation indicates that within the temperature range ~300K
199 to ~1500K, its C_p includes only C_v and anharmonic contributions. The Grüneisen parameter for the
200 pyroxenes and this ring silicate are effectively the same, demonstrating that structural variability
201 has no appreciable effect on the parameter.

202 **Li_2SiO_3**

203 The crystal is an orthorhombic chain silicate with Si_2O_6 chains linked by LiO_4 polyhedra
204 (Hesse, 1977). Experimental $C_p(\text{av})/n$ values ($n=6$) of Téqui et al. (1992) are plotted on Figure 3d
205 (open circles). The C_v contribution was calculated with $\theta = 950\text{K}$ (Fig. 3d, dashed curve) and C_p
206 was calculated (Eq. 3) with α_v given in Figure 2e and a Grüneisen parameter = 1.1 (Fig. 3d, solid
207 curve). It conforms to the experimental data between ~500K and ~700K but systematically
208 underestimates C_p at 900K and greater temperatures. There are three likely reasons for the
209 discrepancy; the value for α_v or C_v is incorrect at high temperature, or γ is greater than 1.1. An

210 incorrect α_V is unlikely in that it was accurately measured and behaves systematically with
211 temperature (Fig. 2e). That C_V would be incorrect at temperatures greater than $\sim 900\text{K}$ also seems
212 unlikely because all C_V values tend toward the same $3nR$ limit (i.e., θ has little effect on C_V at high
213 temperature). This leaves the Grüneisen parameter. An extreme value of 1.3 was adopted for the
214 Grüneisen parameter (Table 2) and C_p was recalculated with the results plotted as a dotted curve
215 on Figure 3d. The C_p discrepancy is diminished but nevertheless remains at temperatures greater
216 than $\sim 1000\text{K}$. Noting that $\gamma = 1.1$ for the previously treated metasilicates, there is no reason to
217 expect a different value for Li_2SiO_3 and we suggest that there is a third, weak contribution to C_p of
218 Li_2SiO_3 at high temperature. We return to this aspect subsequently.

219 **Na_2SiO_3**

220 Na_2SiO_3 is a chain silicate isostructural with Li_2SiO_3 . The crystal undergoes a polymorphic
221 transition (from $Cmc\ 2_1$ symmetry to $Pmc\ 2_1$ symmetry) at $\sim 850\text{K}$ involving Na-O polyhedra but
222 the Q^2 chains are unaffected (Richet et al., 1996). Heat content data from three sources are plotted
223 on Figure 3e. Naylor (1945) used $T^* = 298.15$ whereas Richet et al. (1984) used $T^* = 273.15$ and
224 their different procedures resulted in a systematic difference in $C_p(\text{av})$. To standardize the data,
225 $C_p(\text{av})$ was calculated for both sets of data and the difference between them was $15\text{ Jmol}^{-1}\text{K}^{-1}$ at
226 $\sim 1080\text{K}$. The Richet et al. (1984) $C_p(\text{av})$ values were increased by this amount making the two sets
227 of data remarkably consistent (Fig. 3e). They are also consistent with those reported by Kelley
228 (1960).

229 Na_2SiO_3 C_V values were obtained using $\theta = 750\text{K}$ (Fig. 3e, dashed curve) and C_p was
230 calculated via Equation (3) using α_V provided in Figure 2b and a Grüneisen parameter = 1.1. (Fig.
231 3e, solid curve). The calculated and experimental C_p values are consistent between ~ 300 and
232 $\sim 700\text{K}$ but they diverge beyond $\sim 700\text{K}$. At $\sim 1200\text{K}$ the C_p discrepancy is $\sim 15\%$ relative to the

233 experimental value. There is no obvious effect on C_p at the polymorphic transition ($\sim 850\text{K}$) as
234 shown in Figures 2b or 3e so that any effect of the transition on C_p is within experimental
235 uncertainty. It is concluded that there is a third contribution to the C_p of Na_2SiO_3 with onset at
236 $\sim 700\text{K}$ and this contribution increases systematically with temperature.

237 **K_2SiO_3**

238 K_2SiO_3 , like pseudowollastonite, consists of three-membered rings (Si_3O_9), with potassium
239 polyhedra linking them to produce a monoclinic unit cell (Werthmann and Hoppe, 1981). The heat
240 contents of Beyer et al. (1979) were employed to calculate $C_p(\text{av})/n$ values and these are plotted on
241 Figure 3f (crosses). The results mimic the experimental data for Na_2SiO_3 (Fig. 3f, circles). The
242 melting temperature of K_2SiO_3 is 1195K and the $C_p(\text{av})/n$ experimental datum point at 1150K is
243 much greater than the value at 1100K , which may indicate a premelting region for K_2SiO_3 . A $\theta_D =$
244 750 was employed to calculate C_v of the crystal and it fits reasonably the $C_p(\text{av})/n$ experimental
245 result at $\sim 500\text{K}$ (Fig. 3f) but underestimates $C_p(\text{av})/n$ at greater temperatures. No value for α_v was
246 found for K_2SiO_3 so that C_p could not be calculated and the α_v value of Na_2SiO_3 was used as a
247 proxy, yielding the solid curve of Figure 3f. The agreement with the experimental data in the range
248 $\sim 450\text{-}700\text{K}$ indicates that the α_v proxy is reasonable but the calculated C_p/n values underestimate
249 experimental values at temperatures greater than $\sim 700\text{K}$. No reasonable value of α_v can reproduce
250 the experimental data at high temperature and apparently there is a third contribution to C_p of
251 K_2SiO_3 which is similar in character and magnitude to that of the Na_2SiO_3 C_p discrepancy.

252 **EXPLANATION FOR C_p DISCREPANCIES**

253 **Introduction**

254 Free translation of atoms through crystals is unlikely and electronic contributions to C_p of
255 insulators are similarly unimportant in the temperature range $\sim 300\text{K}$ to 1500K (Slater, 1963; Borg

256 and Dienes, 1992). Substitutional disorder resulting from exchange of cations on different
257 structural sites is also impossible for Na_2SiO_3 , K_2SiO_3 , $\text{Na}_2\text{Si}_2\text{O}_5$ or Li_2SiO_3 unless Si sites are
258 involved, which is highly unlikely. The C_p discrepancies observed for these alkali-bearing crystals
259 therefore arise from other contributions. Heat capacity is the sum of numerous internal and
260 configurational contributions (Grimvall, 2001):

$$261 \quad C_p(\text{crystal}) = C_p(\text{vibration}) + C_p(\text{defect}) + C_p(\text{rotation}) + C_p(\text{libration}) \quad (6)$$

262 Lattice vibrations and anharmonic contributions are here accounted for by Equation (3). There are
263 no structural changes to Li_2SiO_3 or K_2SiO_3 from 298K to their premelting regions, hence there is
264 no contribution to their C_p resulting from polymorphism. Na_2SiO_3 undergoes a transition at $\sim 850\text{K}$
265 from orthorhombic ($Cmc 2_1$) to a lower symmetry, possibly $Pmc2_1$ (Richet et. al., 1996). There is,
266 however, no discontinuity evident in the C_p trend at this temperature (Fig. 3e) so that any resulting
267 C_p contribution is within the uncertainty associated with the measurements of C_p . The effects of
268 dislocations on C_p are well known to experimentalists, and care special is taken to avoid samples
269 with high dislocation densities through sample selection and treatment (e.g., Richet et al., 1996;
270 Naylor, 1945). This leaves configurational contributions such as point defects and rotation/libration
271 as the most likely causes of the C_p discrepancies.

272 Whether intrinsic defect formation or rotation/libration contributions are responsible for the
273 C_p discrepancies can be assessed by reference to crystalline $\text{Na}_2\text{Si}_2\text{O}_5$, a sheet silicate consisting of
274 Q^3 species. Naylor (1945) reports $\text{Na}_2\text{Si}_2\text{O}_5$ heat contents from which $C_p(\text{av})/n$ values were
275 calculated and the results are plotted on Figure 4 (filled circles). The $C_p(\text{av})/n$ data for Na_2SiO_3 are
276 also plotted (Fig. 4, open and shaded circles). The $\text{Na}_2\text{Si}_2\text{O}_5$ and Na_2SiO_3 experimental data are
277 effectively coincident from $\sim 300\text{K}$ to $\sim 1000\text{K}$ and the Debye Function reproduces well the
278 experimental C_p data for $\text{Na}_2\text{Si}_2\text{O}_5$ between 300 and 600K with $\theta_D = 750$ (Fig. 4, dashed curve).

279 The anharmonic contribution to C_p of $\text{Na}_2\text{Si}_2\text{O}_5$ could not be calculated for lack of a α_V value and
280 the Na_2SiO_3 value (Fig. 2b) was used as a proxy to obtain the solid curve of Figure 4. The C_p/n vs.
281 T trend described by the $\text{Na}_2\text{Si}_2\text{O}_5$ experimental data is too steep to be accounted for by Equation
282 (3) using a reasonable value for α_V . We conclude that $\text{Na}_2\text{Si}_2\text{O}_5$ displays a C_p discrepancy of the
283 same magnitude as that for Na_2SiO_3 .

284 The structures of the two crystals are different (chain vs sheet) and the Q^2 and Q^3 tetrahedra
285 of the respective crystals should make different rotational or librational contributions to C_p due to
286 their different linkages. There is, nevertheless a remarkable similarity in the C_p of the two crystals
287 and in their C_p discrepancies. We conclude that rotation and libration are unlikely to be responsible
288 for the similarities in their C_p discrepancies. Instead, the essentially coincidence of the $\text{Na}_2\text{Si}_2\text{O}_5$
289 and Na_2SiO_3 C_p trends relate to their common cation, and specifically to intrinsic cation defect
290 formation in both phases. Although rotation and libration occur in some silicates (Voronko et al.,
291 2006; George et al., 1998; Ghose et al., 1986; Massa et al., 1983) defect formation is the cause of
292 C_p discrepancies in these crystals.

293 **Cation Mobility, Disorder and Relationship to C_p**

294 **Li Mobility in Li_2SiO_3 .** There is experimental evidence for Li mobility in Li_2SiO_3 where
295 subjected to strong thermal agitation. George et al. (1998) conclude from their ^7Li NMR results
296 that: “ Li^+ site hopping is clearly observed in Li_2SiO_3 by a partial averaging of the ^7Li quadrupolar
297 peak shape, requiring exchange among a few, ordered orientations of LiO_4 tetrahedra”. Clearly, Li
298 is not sufficiently mobile, even at 1420K, to have a completely averaged, isotropic environment.
299 With Li-O bond dissociation at high temperature, the majority of mobile Li^+ alight on previously
300 vacated structural sites and re-establish Li-O bonds, which results in no net change to C_p . The
301 spectroscopic results do not preclude, however, a small fraction of mobile Li^+ from having

302 alighted, fleetingly, on interstitial sites to form a few intrinsic (Frenkel) defects. The fraction
303 should increase with temperature as more Li become mobile.

304 **Na Mobility in Na₂SiO₃.** George et al. (1998) observe that Na is strongly mobile in
305 Na₂SiO₃ at high temperatures. Quoting George et al. (1998): “From ²³Na NMR results, Na⁺ site
306 hopping in Na₂SiO₃ appears to involve a more liquid-like behavior, implying exchange among
307 many sites with different orientations in a disordered fashion”. The disordering probably results
308 from a fraction of mobile Na⁺ alighting on interstitial sites to create intrinsic Frenkel defect pairs,
309 as observed for Ca²⁺ in diopside and pseudowollastonite (see next section). These defects increase
310 the C_p of the crystal in proportion to the number of mobile ions at any instant.

311 Insight into the high temperature ‘liquid-like’ behaviour of Na⁺ in Na₂SiO₃ may be gleaned
312 by analogy with Na⁺ behaviour in Na-silicate glass. Although there is some ambiguity in
313 distinguishing different types of cationic sites in the glass, Cormack et al. (2002) nevertheless
314 distinguish ‘cationic sites’ from more energetic ‘transitional sites’, the distinction being dependent
315 on the residence time of the cation on each type of site. Consider, in an energetic sense, the
316 ‘cationic sites’ of the glass to be analogous to the cationic structural sites of the crystal and the
317 ‘transitional sites’ of the glass to be analogous to interstitial sites of the crystal. Cormack et al.
318 (2002) note that Na⁺ of the glass mostly occupies ‘cationic sites’, but during transit from one
319 cationic site to another, the cation may occupy, fleetingly, ‘transitional sites’ (i.e., in Fig. 5 of
320 Cormack et al., 2002; the Na⁺ atom in cation site 1 migrates to a transitional site with its 3rd step).
321 The potential energy minima of ‘transitional sites’ almost certainly are shallower than the minima
322 of the ‘cationic sites’. Occupation of ‘transitional sites’ consequently increases C_p of the glass by
323 an amount proportional to the number of transitional sites occupied at any instant, just as
324 occupation of interstitial (defect) sites in the crystal increases its C_p in proportion to the number of

325 defects present at any instant.

326 **Ca Mobility in Diopside and Pseudowollastonite.** There is very strong experimental
327 evidence for Ca mobility in diopside and pseudowollastonite at temperatures greater than ~1500K
328 (Bouhfid et al., 2002; Dimanov and Jaul, 1998; Dimanov and Ingrin, 1995). Based on Rutherford
329 Backscattering analysis Dimanov and Ingrin (1995) observed a high temperature intrinsic diffusion
330 regime in diopside which “takes place near the onset of premelting as detected in calorimetric
331 measurements and can be interpreted in terms of enhanced formation of Frenkel defects”. The
332 premelting region commences at 1500-1600K. These results were confirmed by Dimanov and Jaul
333 (1998) who also concluded that Ca self-diffusion may involve Ca-Frenkel point defects. The
334 Raman and conductivity experiments of Bouhfid et al. (2002) demonstrated the mobility of Ca in
335 both pseudowollastonite and gehlenite, where mobility of Ca in the two phases occurs at
336 temperatures greater than ~1500K. The Ca-Frenkel defects formed will contribute to the C_p of
337 these crystals but only at temperatures above ~1500K (i.e., in their premelting regions).

338 **C_p Discrepancies and Cation-O Bond Strengths**

339 The mobility of cations and the abundance of intrinsic cation defects increase with
340 temperature because thermal agitation promotes rupture of cation-oxygen bonds. There may be,
341 therefore, a relationship between cation-oxygen bond dissociation energies, cation mobility, defect
342 formation and C_p -discrepancies. K-O and Na-O bond dissociation energies are weak at 239 kJ/mol
343 and 257 kJ/mol respectively whereas the Li-O bond is somewhat stronger at 341 kJ/mol (Speight,
344 2005). The alkaline earth-oxygen bond dissociation energies are stronger still, ranging between
345 394 and 563 kJ/mol. From these values we conclude that dissociation of K-O and Na-O bonds
346 should occur at comparatively low temperatures, Li-O dissociation at somewhat greater
347 temperature and Mg-O and Ca-O bond dissociation should occur at still greater temperatures. The

348 Na and K metasilicate and disilicate C_p discrepancies commence at ~700-800K and their C_p
 349 discrepancies are the most pronounced (Figs. 3, 4). The Li metasilicate C_p discrepancy (Fig. 3d)
 350 commences at greater temperature (900-1000 K), and it is less pronounced than the discrepancies
 351 for Na and K silicates (Figs. 3d 3e, 3f). Finally, no C_p discrepancies are apparent up to 1500K for
 352 the alkaline earth metasilicates (Figs. 3a, 3b, 3c). Bond dissociation energies correlate well with
 353 the temperatures at which C_p discrepancies are initiated and with the strength of the discrepancies.
 354 We propose that bond dissociation, resulting from strong thermal agitation, promotes cation
 355 mobility, cation (Frenkel) defect formation and production of the C_p discrepancies of the alkali
 356 metasilicates (Figs. 3 and 4). The same order of bond strength ($K_2O < Na_2O < Li_2O < MgO/CaO$) is
 357 obtained from Coulombic interaction considerations using effective ionic radii (Huheey et al.,
 358 1993, Chap. 4).

359 **Reactions Producing Defects and C_p Discrepancies**

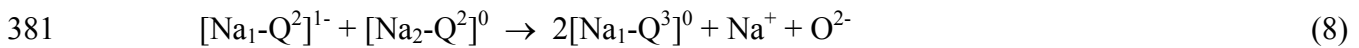
360 **Cationic Defects.** We have concluded that Na-NBO bond dissociation is observed in
 361 crystalline Na_2SiO_3 above ~700-800K (see also Nesbitt et al., 2017) and the reaction proceeds
 362 according to:



364 where $[Na_2-Q^2]^0$ is a Q^2 species with a Na atom bonded to each NBO, and $[Na_1-Q^2]^{1-}$ represents a
 365 Q^2 species where one NBO has no associated Na atom. With NBO-M bond dissociation, the cation
 366 (M) vacates its structural site and migrates to a non-structural (interstitial) site. The escape of Na^+
 367 from a structural site creates a vacancy, and together with the occupation of a non-structural site,
 368 creates a *Frenkel* defect pair. Creation of these defects increases the C_p of the crystal (i.e., the C_p
 369 discrepancy) and consequently increases the entropy of the crystal (Courtial et al., 2000; Richet et
 370 al., 1998; Dimanov and Ingrin, 1995). These contributions are *configurational* in nature, and are a

371 major contributor to the C_p discrepancies observed in Figures 3d, 3e, 3f and 4. The cation defects
372 must be located between the Q^2 chains thus weakening forces binding the chains together.

373 **Anionic Defects.** With formation of a $[Na_1-Q^2]^{1-}$ moiety via Reaction (7), the tetrahedron
374 becomes ‘unpinned’ at its NBO^- apex (i.e., the apex with no associated Na^+). Due to thermal
375 agitation it may undergo librations different from, and more severe than, ‘pinned’ $[Na_2-Q^2]^0$
376 moieties. George et al. (1998) corroborate the effects of thermal agitation, noting that there is
377 “some kind of extensive, librational motion of SiO_4 tetrahedral” in crystalline Na_2SiO_3 at high
378 temperature. As emphasized by Nesbitt et al. (2017), the $[Na_1-Q^2]^{1-}$ moiety produced by Reaction
379 (7) is a nucleophile which may attack Si centers of Q^2 species resident on adjacent chains. The
380 reaction produces Q^3 species ($[Na_1-Q^3]^0$) according to:



382 where O^{2-} is free oxygen or the oxide ion (Nesbitt et al., 2017, their Rxn 2b). The presence of Q^3
383 species in the Raman spectra of Na_2SiO_3 confirms that Reaction (8) occurs at temperatures as low
384 as 774K (Richet et al., 1996). The O^{2-} produced must also form anionic Frenkel pairs because
385 Reaction (8) annihilates a tetrahedral oxygen site through formation of BO. Wherever O^{2-} alights it
386 will occupy an interstitial site. It may reside on sites with weak potential energy minima associated
387 with cationic polyhedra (located between Q^2 chains) or it may react with other moieties of the
388 crystal, as discussed in the next paragraph. The abundance of cationic Frenkel defects is at least
389 double the abundance of anionic Frenkel defects (see Eqns. 7 and 8)

390 The strong nucleophile, O^{2-} , is a highly reactive, strong nucleophile and some O^{2-} may
391 attack Q species to produce Si-pentahedra (SiO_5) such as observed in alkali silicate glasses and
392 melts (e.g., Bereznoi and Boiko, 2005; Stebbins, 1991). The SiO_5 moiety then becomes the
393 defect. At high temperatures the lifetimes of all Si tetrahedra are short (Farnan and Stebbins, 1990)

394 as will be the lives of the SiO_5 moieties. The activation energy associated with formation of the
395 SiO_5 moiety may inhibit its production at low temperatures. Nevertheless, the anionic defects O^{2-}
396 or SiO_5 necessarily contribute to $C_p(\text{config.})$.

397 **Defects in Other Alkali Silicate Crystals.** The K-O bond dissociation energy is less than
398 that of Na-O so that reactions equivalent to (7) and (8) likely occur in crystalline K_2SiO_3 (and
399 $\text{K}_2\text{Si}_2\text{O}_5$). By analogy with Na-NBO bond dissociation in Na_2SiO_3 , K-NBO dissociation should
400 occur at $\sim 700\text{-}800\text{K}$ with intrinsic cationic point defects forming in the K-silicate crystals, thus
401 explaining the C_p deficiency observed in Figure 3f. The Li-O bond strength is greater than Na-O
402 bond strength so that Li cation point defect formation should be inhibited in Li_2SiO_3 relative to
403 Na_2SiO_3 . The prediction holds in that Li_2SiO_3 displays a weaker C_p discrepancy than Na_2SiO_3 and
404 the discrepancy is restricted to higher temperatures, commencing at $\sim 900\text{-}1000\text{K}$ (Fig. 3d). There
405 is no evidence that Reaction (2) occurs in Li_2SiO_3 (Richet et al., 1996), hence there is no evidence
406 for appreciable O^{2-} disorder in Li_2SiO_3 . Finally, based on Na disorder in Na_2SiO_3 , Na-O bond
407 dissociation and cation defects formation probably occurs in $\text{Na}_2\text{Si}_2\text{O}_5$ above $\sim 700\text{K}$, accounting
408 for the C_p discrepancy observed in Figure 4.

409 **Defect Abundances in Na_2SiO_3**

410 Creation of Q^3 species via Reaction (2) annihilates Na and O structural sites and the
411 displaced atoms must reside on other sites, here considered ‘defect’ sites. Production of Q^1 species
412 creates new Na and O structural sites by establishment of additional Si-NBO-Na moieties (Nesbitt
413 et al., 2017, their Reaction 3). The 1348K Raman spectrum of Na_2SiO_3 collected by Richet et al.
414 (1996) was fit by Nesbitt et al. (2017) to obtain $\sim 10\%$ Q^1 species, $\sim 68\%$ Q^2 species and $\sim 22\%$ Q^3
415 species. These Q species abundances were used to calculate the abundance of O^{2-} , yielding ~ 1.7
416 mol% O^{2-} or $X_{\text{O}^{2-}} = 0.017$ (see Sawyer et al., 2015, Appendix A for calculation). Considering that

417 there are 3 moles of O per unit formula, there exists 0.051 (3x0.017) moles of O²⁻ in the crystal.
418 Reactions (7) and (8) combined indicate twice the moles of ‘defect’ Na (i.e., Na*) as O²⁻, requiring
419 0.102 moles of Na* in the crystal at 1348K. But there are two moles of Na per unit formula so that
420 $X_{Na^*} = 0.051$. Richet et al. (1996) also collected and fit Na₂SiO₃ Raman spectra at 1217K and
421 965K. Q¹ species were absent and Q³ species were present at ~10% and ~5% respectively (visual
422 estimates), indicating that $X_{Na^*} \sim 0.025$ and $X_{O^{2-}} \sim 0.016$ at 1217K, and $X_{Na^*} \sim 0.012$ and $X_{O^{2-}}$
423 ~ 0.008 at 965K. The Q³ signal is undetectable in Raman spectra below 774K (Richet et al., 1996),
424 the implication being that Na* and O²⁻ are negligible below this temperature.

425 Reaction (7) creates a cationic vacancy and interstitial site (i.e., a Frenkel pair) whereas
426 Reaction (8) annihilates a cationic site by a different mechanism (Nesbitt et al., 2017). Thus the
427 abundance of Frenkel pairs is that produced by Reaction (7), which represents half the X_{Na^*}
428 calculated in the previous paragraph. The values of X_{Na^*} therefore were halved to obtain the
429 number of Frenkel pairs produced by Reaction (7) and these are plotted on Figure 5 (solid circles).
430 The equation appropriate to prediction of Frenkel pairs is (Borg and Dienes, 1992):

$$431 \quad \ln(X_{Na^*}) = -E^*/(2RT) \quad (3)$$

432 where E* is the energy required to create the vacancy site-interstitial site pair, R is the gas constant
433 and T is temperature (K). With E* = -84560 J/mol, the calculated increase in X_{Na^*} as a function of
434 temperature is illustrated by the solid curve (Fig. 5), which agrees reasonably with the
435 experimental values at 965K, 1217K and 1348K (Fig. 5, solid circles). The calculation indicates
436 that $X_{Na^*} \sim 0.001$ at 700K. The calculation indicates that a C_p discrepancy for Na₂SiO₃ should be
437 vanishingly small up to ~700K (Fig. 3e). Beyond 700K Na* concentrations increase rapidly with
438 temperatures, as does the C_p discrepancy of Na₂SiO₃. The calculations are consistent with the
439 Raman spectral results (Richet et al., 1996) and with C_p measurements (Fig. 3e). Raman spectra of

440 Li_2SiO_3 reveal no obvious Q^3 species up to 1465K (Richet et al., 1996), indicating an absence of
441 O^{2-} . The very weak C_p discrepancy beginning at ~900-1000K (Fig. 3d) likely is attributed solely to
442 minor Li disorder (e.g., Frenkel pair formation). There are insufficient experimental data to
443 calculate cation defect abundances for the other alkali silicates.

444 **IMPLICATIONS FOR MANTLE MINERALS**

445 The observations and deductions concerning C_p indicate that alkali-O bond dissociation and
446 defect formation occur in alkali metasilicate and disilicate crystals due primarily to thermal
447 agitation. Alkali-O bond dissociation energies are low compared with alkaline earth-O bond
448 dissociation energies, implying that greater thermal agitation is required for the latter bonds to be
449 ruptured. The very high temperatures of the mantle may be sufficient to cause alkaline earth-O
450 bond dissociation and to produce defects in pyroxenes and olivines. Dimanov and Ingrin, (1995)
451 Richet et al. (1998), Dimanov and Jaoul (1998) and Bouhifd et al. (2002) documented the
452 enhanced mobility (disorder) of Ca in pseudowollastonite, diopside and gehlenite, where disorder
453 commences at ~1500-1600K in the first two phases and ~1800K for the last. In addition, Mg
454 disordering, hence Mg-O bond dissociation, probably occurs within the premelting region of
455 enstatite and forsterite (Richet et al., 1993; Thiéblot et al., 1999), and likely occurs within the
456 premelting regions of most minerals subjected to mantle temperatures (Richet et al., 1998; 1994;
457 Richet and Fiquet, 1991). Where Ca or Mg disordering occurs in pyroxenes, reactions entirely
458 analogous to Reactions (7) and (8) may occur (with Ca or Mg substituted for 2Na) thus promoting
459 formation of intrinsic, Frenkel type, defects in the minerals. Two implications for mantle minerals
460 follow.

461 The onset of premelting of diopside and proto-enstatite occurs at ~1550K and ~1700K
462 respectively, resulting in cation disorder and formation of Frenkel type cationic defects (Thiéblot

463 et al., 1999; Richet et al. 1998; Dimanov and Ingrin 1995). As here emphasized, the defects tend to
464 destabilize the minerals by increasing their C_p , entropy and free energy values. In response, the
465 minerals may change structure or composition to produce a more stable phase. Structural changes
466 driven by defect formation may include creation of ‘new’ sites which incorporate previously
467 disordered cations. These new structural sites may be accompanied by other changes such as
468 incorporation of Al into octahedral or tetrahedral sites, which should stabilize the minerals at high
469 temperature (Al-O bond dissociation energy is ~ 512 kJ/mol). Through such changes, the
470 abundance of point defects should decrease, thereby stabilizing pyroxenes against the effects of
471 thermal agitation. The Ca-Tschermak ($\text{CaAl}_2\text{SiO}_6$) and $\text{NaAlSi}_2\text{O}_6$ components are likely examples
472 of pyroxene components produced through minimization of cationic defects. We suggest that
473 elimination of defects through changes to composition and structure play an important role in
474 stabilizing pyroxenes against extreme thermal agitation.

475 Richet et al. (1993) suggests that Mg undergoes disordering within the premelting region of
476 forsterite (~ 2050 - 2163 K) which spans the temperature range of the wadsleyite stability field
477 (Frost, 2008; Katsura et al., 2004). Mg-O bond dissociation and production of Frenkel defects
478 should contribute to the instability of olivine and to formation of wadsleyite by converting the
479 highly energetic Mg Frenkel defects of olivine to more stable edge-sharing Mg^{2+} octahedral
480 structural sites of wadsleyite (Ashbrook et al., 2005). In addition, Mg-O bond dissociation
481 necessarily produces a negatively charged $[\text{Q}^0]^-$ moiety within the crystal (e.g., Nesbitt et al.,
482 2017). The moiety is a strong nucleophile and due to thermal agitation it may encounter and react
483 with adjacent Q^0 species to produce a $[\text{Si}_2\text{O}_6]$ moiety and O^{2-} according to:



485 The reaction is analogous to Reaction (4) and occurs in Mg_2SiO_4 glass and melt in which Q^1

486 species are observed (Nesbitt et al., 2015; Sen and Tangeman, 2008; Voronko et al., 2006). The
487 products of Reaction (4), Q^1 and O^{2-} , are essential constituents of wadsleyite, β - Mg_2SiO_4 ,
488 (Ashbrook et al., 2005) and the reaction should promote its formation at the expense of olivine.
489 The presence of wadsleyite in the mantle may have as much to do with Mg-O bond dissociation
490 (through thermal instability) and production of Q^1 species and O^{2-} in olivine as it has to do with
491 pressure.

492 **ACKNOWLEDGEMENTS**

493 The authors acknowledge the logistical support provided by their associated Universities.
494 We thank Dr. G.M. Bancroft for numerous fruitful discussions and encouragement. We gratefully
495 acknowledge P. Richet, his colleagues and associates for their remarkably detailed measurements
496 of the high temperature properties of alkali and alkaline earths silicates.

497 **References**

- 498 Anderson, O.L. (1967) Equation for thermal expansivity in planetary interiors. *Journal of*
499 *Geophysical Research*, 72, 3661–3668.
- 500 Angel, R.J., and Jackson, J.M. (2002) Elasticity and equation of state of orthoenstatite, $MgSiO_3$.
501 *American Mineralogist*, 87, 558-561.
- 502 Ashbrook, S.E., Berry, A.J., Hibberson, W.O., Steuernagel, S., and Wimperis, S. (2005) High-
503 resolution ^{17}O MAS NMR spectroscopy of forsterite (α - Mg_2SiO_4), wadsleyite (β - Mg_2SiO_4),
504 and ringwoodite (γ - Mg_2SiO_4). *American Mineralogist*, 90, 1861-1870.
- 505 Bereznoi, G.V., and Boiko, G.G. (2005) Defects and Oxygen Diffusion in Metasilicate Melts,
506 *Molecular Dynamics Simulation, Glass Physics and Chemistry*, 31, 145 -154.
- 507 Beyer, R.P., Ferrante, M.J., Brown, R.R., and Daut, G.E. (1979) Thermodynamic properties of
508 potassium metasilicate and disilicate, United States Bureau of Mines, Report of Investigations,

509 8410.

510 Borg, R.J., and Dienes, G.J. (1992) *The Physical Chemistry of Solids*. Academic Press Inc.,
511 Boston, 584 p.

512 Born, M., and von Kármán, (1912) Über Schwingungen in Raumgittern. *Phys. Zeits.*, **13**, 297-309.

513 Bouhfid, M.A., Gruener, G., Mysen, B.O., and Richet, P. (2002) Premelting and calcium mobility
514 in gehlenite ($\text{Ca}_2\text{Al}_2\text{SiO}_7$) and pseudowollastonite (CaSiO_3). *Physics and Chemistry of*
515 *Minerals*. 29, 655-662.

516 Chopelas, A., (2000) Thermal expansivity of mantle relevant magnesium silicates derived from
517 vibrational spectroscopy at high pressure. *American Mineralogist*, 85, 270-278.

518 Cormack, A.N., Du, J., and Zeitler, T.R. (2002) Alkali ion migration mechanisms in silicate
519 glasses probed by molecular dynamics simulations. *Physical Chemistry and Chemical*
520 *Physics*, 4, 3193-3197.

521 Courtial, P., Téqui, C. and Richet, P. (2000) Thermodynamics of diopside, anorthite,
522 pseudowollastonite, CaMgGeO_4 olivine, and åkermanite up to near the melting point.
523 *Physics and Chemistry of Minerals*, 27, 242-250.

524 Debye, P. (1912) Zur theorie der spezifischen warmen. *Ann. d. Physik.*, **39**, 789-839.

525 Dimanov, A., and Ingrin, J. (1995) Premelting and High-Temperature Diffusion of Ca in Synthetic
526 Diopside: An Increase of the Cation Mobility. *Physics and Chemistry of Minerals*, 22, 437-
527 442.

528 Dimanov, A., and Jaoul, O. (1998) Calcium self-diffusion in diopside at high temperature:
529 implications for transport properties. *Physics and Chemistry of Minerals*, 26, 116-127.

530 Einstein, A. (1907) Die plancksche theorie der strahlung und die theorie der spezifischen warmen.
531 *Ann. d. Physik.* **22**, 180-190.

532 Farnan, I., and Stebbins, J.F. (1990) High-temperature ^{29}Si NMR investigation of solid and molten
533 silicates. *Journal of the American Chemical Society*, 112, 32-39.

534 Frost, D. (2008) The upper mantle and transition zone. *Elements*, 4, 171-176.

535 George, A.M., Richet, P., Stebbins, J.F. (1998) Cation dynamics and premelting in lithium
536 metasilicate (Li_2SiO_3) and sodium metasilicate (Na_2SiO_3): A high-temperature NMR study.
537 *American Mineralogist*, 83, 1277-1284.

538 Ghose, S., Choudhury, N. Chaplot, S.L., and Rao, K.R. (1991) Phonon Density of States and
539 Thermodynamic Properties of Minerals. Chapter 11, in *Thermodynamic Data: Systematics
540 and Estimation*. (S.K. Saxena ed.), p. 283-314. Springer-Verlag, New York, 367 p.

541 Ghose, S., Schomaker, V., and McMullan, R.K. (1986) Enstatite, $\text{Mg}_2\text{Si}_2\text{O}_6$: A neutron diffraction
542 refinement of the crystal structure and a rigid-body analysis of the thermal vibration.
543 *Zeitschrift für Kristallographie*, 176, 159 -175.

544 Grimvall, G. (2001) Dependence of Thermodynamic Properties on Atomic Masses and Bonding in
545 Solids. Chapter 2, in *Solid Solutions in Silicate and Oxide Systems*, ed. C.A. Geiger, v3,
546 p11-36. Eötvös University Press, Budapest.

547 Grüneisen, E. (1912) Theorie des festen Zustandes einatomiger Elemente. *Ann. Phys.* **39**, 257-306.

548 Grüneisen, E (1926) Zustand des festen Körpers. *Handbuch Phys.*, **1**, 1-52.

549 Hesse, K.F. (1977) Refinement of the crystal structure of lithium polysilicate. *Acta*
550 *Crystallographica B* 33:901-902.

551 Hofmeister, A.M., and Mao, H-K (2002) Redefinition of the mode Grüneisen parameter for
552 polyatomic substances and thermodynamic implications. *Proceedings of the National
553 Academy of Sciences*, 99, 559-564.

554 Huheey, J.E., Keiter, E.A., and Keiter, R.L. (1993) *Inorganic Chemistry*. Harper-Collins College

555 Publishers, New York, 964 p.

556 Ita, J., and Stixrude, L. (1992) Petrology, Elasticity, and Composition of the Mantle Transition
557 Zone. *Journal of Geophysical Research*, 97, 6849-6866.

558 Jackson, J.M., Palko, J.W., Andrault, D., Sinogeikin, S.V., Lakshtanov, D.L., Wang, J., Bass, J.D.,
559 and Zha, C-S. (2003) Thermal expansion of natural orthoenstatite to 1473 K. *European*
560 *Journal of Mineralogy*, 15, 469-473.

561 Jeanloz, R., and Thompson, A.B. (1983) Phase transitions and mantle discontinuities. *Reviews of*
562 *Geophysics and Space Physics*, 21, 51-74.

563 Katsura, T., Yamada, H., Nishikawa, O., Song, M., Kubo, A., Shinmei, T., Yokoshi, S., Aizawa,
564 Y., Yoshino, T., Walter, M.J., Ito, E., and Funakoshi, K. (2004) Olivine-wadsleyite
565 transition in the system (Mg,Fe)₂SiO₄. *Journal of Geophysical Research*, 109, B02209 1-12.

566 Kelley, K.K. (1960) Contribution to the data on theoretical metallurgy: XII. High-temperature heat
567 content, heat-capacity and entropy data for the elements and inorganic compounds. Bureau
568 of Mines Bulletin 584. United States Government Printing Office, Washington, 163 p.

569 Kieffer, S.W. (1980) Thermodynamics and Lattice Vibrations of Minerals: Application to Chain
570 and Sheet Silicates and Orthosilicates. *Reviews of Geophysics and Space Physics*. 18, 862-
571 886.

572 Kieffer SW (1982) Thermodynamics and lattice vibrations of minerals: 5. Applications to phase
573 equilibria, isotopic fractionation, and high-pressure thermodynamic properties. *Reviews of*
574 *Geophysics and Space Physics* 20, 827-849.

575 Krupka, K.M., Hemingway, B.S., Robie, R.A., and Kerrick, D.M. (1985) High-temperature heat
576 capacities and derived thermodynamic properties of anthophyllite, diopside, dolomite,
577 enstatite, bronzite, talc, tremolite, and wollastonite. *American Mineralogist*, 70, 261-271.

578 Massa, N.E., Ullman, F.G., and Hardy, J.R. (1983) Interpretation of anomalies in the Raman
579 spectrum of K_2SeO_4 in terms of oxygen sublattice disorder. *Physical Review B*, 27, 1523-
580 1540.

581 Naylor, B.F. (1945) High-temperature heat contents of sodium metasilicate and sodium disilicate.
582 *Journal of the American Chemical Society*, 67, 466-467.

583 Nesbitt, H.W., Bancroft, G.M., Henderson, G.S., Sawyer, R., Secco, R.A., (2015). Direct and
584 Indirect Evidence for Free Oxygen (O^{2-}) in MO-Silicate Glasses and Melts (M = Mg, Ca,
585 Pb). *Am. Mineral.* 100, 2566-2578.

586 Nesbitt, H.W., Bancroft, G.M., Henderson, G.S., Richet, P., and O'Shaughnessy, C. (2017)
587 Melting, crystallization and the glass transition: toward a unified description for silicate
588 phase transitions. *American Mineralogist*, 102, 412-420.

589 Pandolfo, F., Cámara, F., Domeneghetti, M.C., Alvaro, M., Nestola, F., Karato, S-I., and Amulele,
590 G. (2015) Volume thermal expansion along the jadeite–diopside join. *Physics and*
591 *Chemistry of Minerals*. 42, 1-14.

592 Pitzer, K.S., and Brewer, L. (1961) *Thermodynamics* (revised after Lewis, G.N., and Randall, M),
593 McGraw-Hill Inc. New York, 723 p.

594 Richet, P., and Fiquet, G. (1991) High-temperature heat capacity and premelting of minerals in the
595 system MgO-CaO- Al_2O_3 - SiO_2 . *Journal of Geophysical Research*, 96, 445-456.

596 Richet, P., Bottinga, Y., and Téqui, C. (1984) Heat capacity of sodium silicate liquids. *Journal of*
597 *the American Ceramics Society*. 67, C6-C8.

598 Richet, P., Ingrin, J., Mysen, B.O., Courtial, P., and Gillet, P. (1994) Premelting effects in
599 minerals: an experimental study. *Earth and Planetary Science Letters*, 121, 589-600.

600 Richet, P., Leclerc, F., and Benoist, L. (1993) Melting of forsterite and spinel, with implications

601 for the glass transition of Mg_2SiO_4 liquid. *Geophysical Research Letters*, 20, 1675-1678.

602 Richet, P., Mysen, B.O., and Andrault, D. (1996) Melting and premelting of silicates: Raman
603 spectroscopy and X-ray diffraction of Li_2SiO_3 and Na_2SiO_3 . *Physics and Chemistry of*
604 *Minerals*. 23, 157-172.

605 Richet, P., Mysen, B.O., and Ingrin, J. (1998) High-temperature X-ray diffraction and Raman
606 spectroscopy of diopside and pseudowollastonite. *Physics and Chemistry of minerals*, 25,
607 401-414.

608 Sawyer, R., Nesbitt, H.W., Bancroft, G.M., Thibault, Y., and Secco, R.A. (2015) Spectroscopic
609 studies of oxygen speciation in potassium silicate glasses and melts. *Canadian Journal of*
610 *Chemistry*, 93, 60–73.

611 Saxena, S.K., Chatterjee, N., Fei, Y., and Shen, G. et al., (1993) *Thermodynamic Data of Oxides*
612 *and Silicates*. Springer-Verlag, Berlin, p. 386-387.

613 Sen, S., and Tangeman, J. (2008) Evidence for anomalously large degree of polymerization in
614 Mg_2SiO_4 glass and melt. *American Mineralogist*, 93, 946-949.

615 Slater, J.C. (1963) *Introduction to Chemical Physics*. McGraw-Hill Book Company Inc. (1st
616 Paperback Edition), New York, 521p.

617 Speight, J.G. (2005) *Lange's Handbook of Chemistry 70th Anniversary Edition*. McGraw Hill
618 *Standard Handbook*, New York, Table 4.11, p. 4.41-4.51.

619 Stebbins, J.F. (1991) NMR evidence for five-coordinated silicon in silicate glass at atmospheric
620 pressure. *Nature*, 351, 638-639.

621 Téqui, C., Grinspan, P., and Richet, P. (1992) Thermodynamic Properties of Alkali Silicates: Heat
622 Capacity of Li_2SiO_3 and Lithium-Bearing Melts. *Journal of the American Ceramic Society*, 75,
623 2601-2604.

624 Thiéblot, L., Téqui, C., and Richet, P. (1999) High-temperature heat capacity of grossular
625 ($\text{Ca}_3\text{Al}_2\text{Si}_3\text{O}_{12}$), enstatite (MgSiO_3), and titanite (CaTiSiO_5). *American Mineralogist*, 84, 848-
626 855.

627 Voronko, Yu. K., Sobol, A.A., and Shukshin, V.E. (2006) Raman Spectra and Structure of Silicon-
628 Oxygen Groups in Crystalline, Liquid, and Glassy Mg_2SiO_4 . *Inorganic Materials*, 42, 981-988.

629 Werthmann, R., and Hoppe, R. (1981) Über K_2SiO_3 – das erste cyclotrisilicat eines alkalimetalls
630 sowie Rb_2SiO_3 , Cs_2SiO_3 , Rb_2GeO_3 und Cs_2GeO_3 . *Revue de Chimie Minérale*, 18, 593-607.

631 Yang, H., and Ghose, S. (1994) Thermal expansion, Debye temperature and Grüneisen parameter
632 in synthetic (Fe, Mg) SiO_3 orthopyroxenes. *Physical Chemistry of Minerals*, 20, 575-586.

633 Zhao, Y., Schiferl, D., and Shankland, T.J. (1995) High P-T single-crystal x-ray diffraction study
634 of thermoelasticity of MgSiO_3 orthopyroxene. *Physics and Chemistry of Minerals*, 22, 393-
635 398.

636 **Figure Captions**

637 **Fig. 1:** (a) Illustrates the heat capacity (at constant pressure) of crystalline and liquid Na_2SiO_3 as a
638 function of temperature. The vertical dotted line represents initiation of the premelting region of
639 the crystal the dotted, curved arrow indicates the trend in C_p within the premelting region. The
640 vertical solid arrow indicates the melting point. (b) Illustrates the normalized heat (C_p/n) of the
641 crystal as a function of temperature (n = no. of atoms in the unit formula). The dashed curve
642 represents C_v (Debye Function) calculated assuming the Debye Temperature = 750K and the
643 dotted arrow indicates the premelting trend.

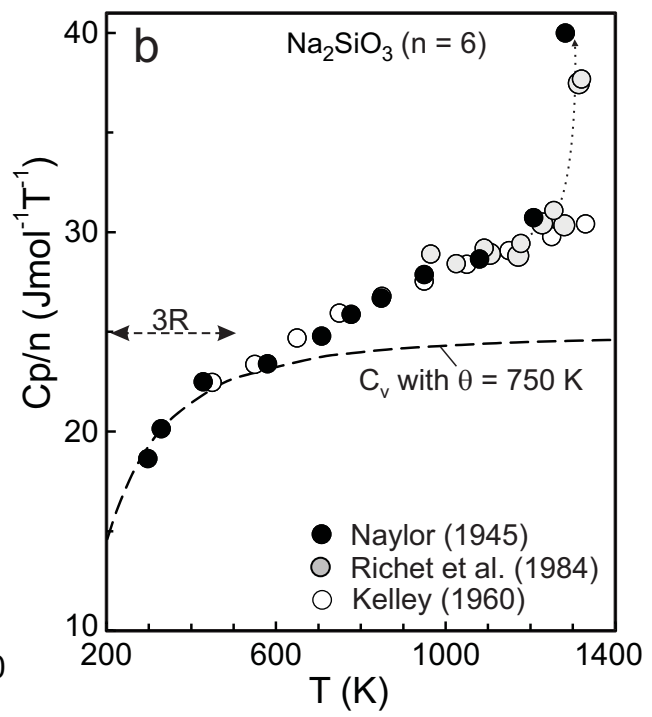
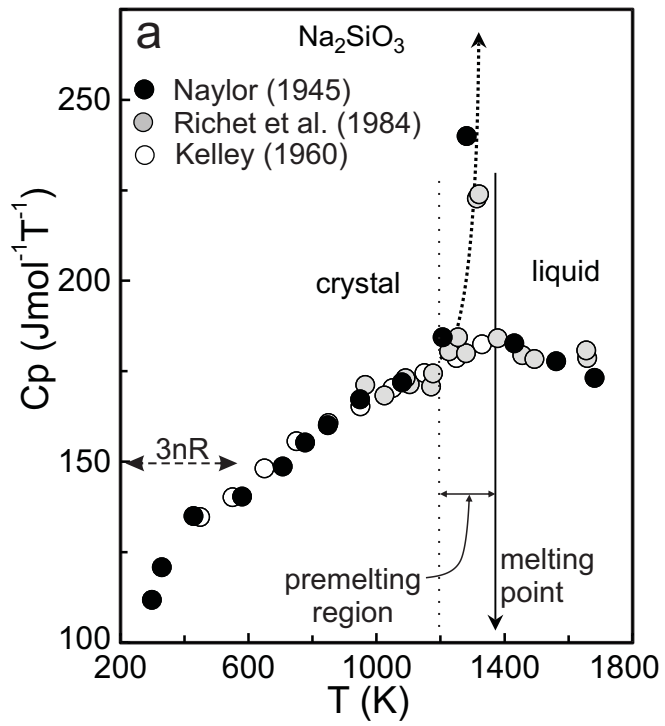
644 **Fig. 2:** Illustrates volumetric properties of some chain and ring silicates as a function of
645 temperature. (a) volume of Na_2SiO_3 (c) as a function of temperature. The straight line is the least
646 squares best fit to the solid circles. The arrow indicates onset of the premelting region. (b), (c), (d),

647 (e) and (f) Illustrates the volume coefficient of thermal expansion (α_V) of the indicated crystal as a
648 function of temperature. The solid curves are a least squares best fit to the solid circles. The best fit
649 equation and the source of the data are provided in each diagram.

650 **Fig. 3:** Illustrates the experimental and calculated 'normalized' C_p results for the indicated crystals
651 (normalized $C_p = C_p/n$ where $n =$ no. of atoms per unit formula). The solid curve in each diagram
652 represents the C_p calculated from Equation (3). The dashed curves represent C_v calculated using
653 the Debye Temperature indicated in the diagram. The short arrow (labelled m.p. in some diagrams)
654 indicates the melting point. The dotted curves indicate the C_p trends within the premelting regions
655 of the crystals. See text for details. (a) C_p/n values for orthoenstatite (small and large circles) and
656 proto-enstatite (shaded circles); (b) C_p/n values for diopside.; (c) C_p/n values for
657 pseudowollastonite (p- CaSiO_3); (d) C_p/n for Li_2SiO_3 (c). The dotted curve represents C_p/n values
658 calculated assuming that the Grüneisen parameter = 1.3. (e) C_p/n of Na_2SiO_3 (c); (f) C_p/n for
659 K_2SiO_3 (c) is indicated by crosses and the C_p/n data for Na_2SiO_3 are indicated by open and shaded
660 circles.

661 **Fig. 4:** Illustrates the experimental C_p/n values for $\text{Na}_2\text{Si}_2\text{O}_5$ (solid circles). The experimental C_p/n
662 values for Na_2SiO_3 are plotted for comparison (open and shaded circles). The dashed curve
663 represents the Debye Function and the two dotted arrows indicate C_p/n trends within the
664 premelting regions of $\text{Na}_2\text{Si}_2\text{O}_5$ and Na_2SiO_3 .

665 **Fig. 5:** Defect concentrations of Na (X_{Na^*}) determined from experiment (dots) and the calculated
666 Frenkel pair defect concentrations (solid curve) using the activation energy shown in the diagram.
667 Details are provided in the text.



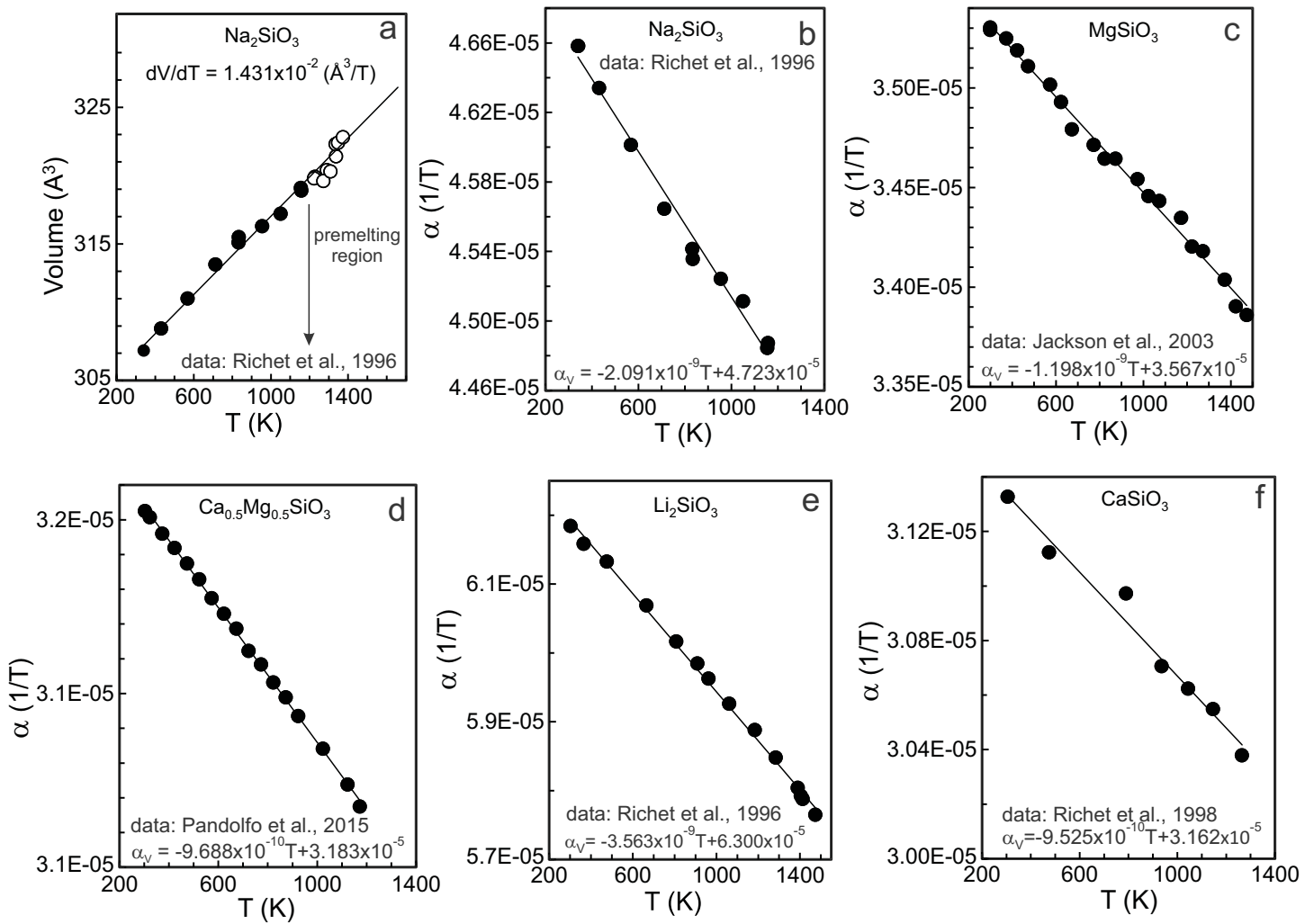


Fig. 2

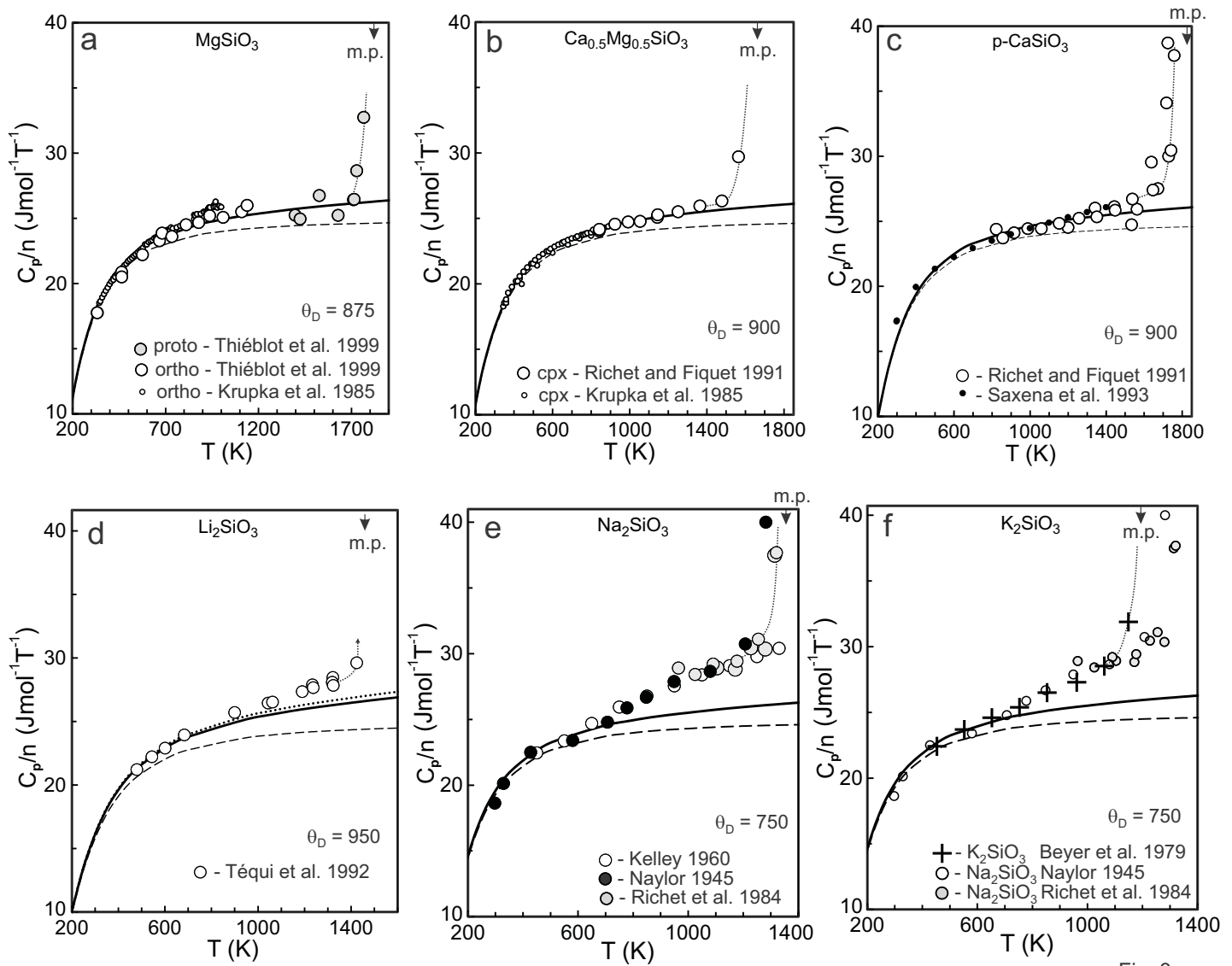


Fig. 3

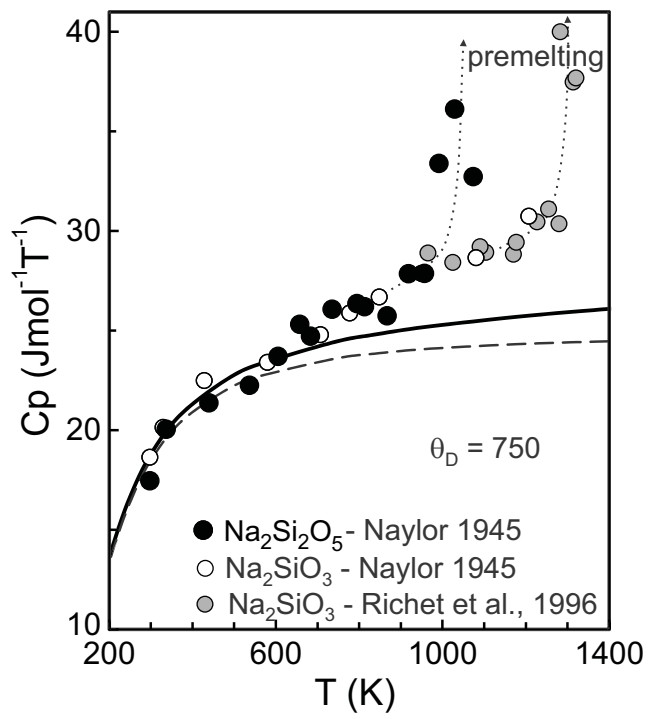


Fig. 4

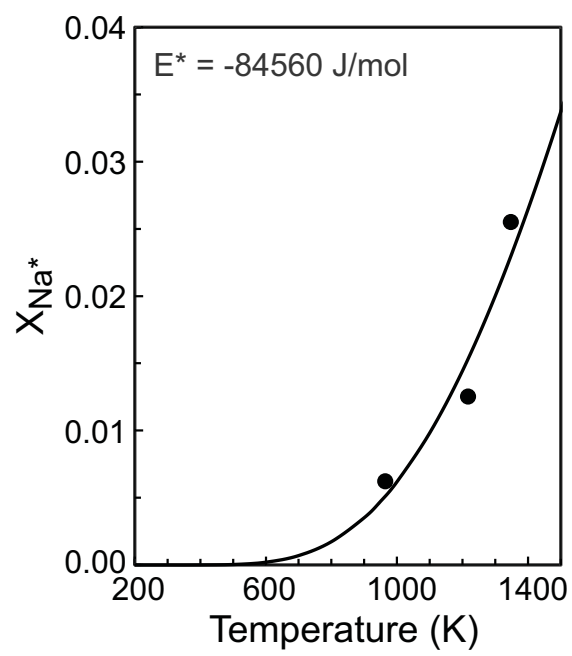


Fig. 5

Table 1: The Debye Function¹

θ/T	T (K)	C_v
	750	$J/mol^{-1}T^{-1}$
0.10	0.0	24.89
0.20	0.0	24.85
0.30	0.0	24.81
0.40	0.0	24.73
0.50	0.0	24.60
0.60	0.0	24.48
0.70	0.0	24.31
0.80	0.0	24.14
0.90	0.0	23.93
1.00	0.0	23.72
1.50	0.0	22.34
2.00	0.0	20.59
2.50	0.0	18.62
3.00	0.0	16.53
3.50	0.0	14.48
4.00	0.0	12.55
5.00	0.0	9.20
6.00	0.0	6.61

¹ Pitzer and Brewer (1961),
Table A5-1, p. 660.

Table 2: Gruneisen Parameter (γ) for Chain Silicates

Phase	Composition	γ	Error	References
Orthopyroxene	(Mg,Fe)SiO ₃	1.1	±0.1	Jeanloz and Thompson, 1983
Orthopyroxene	FeSiO ₃	1.1	?	Anderson, 1967
Orthopyroxene	(Mg,Fe)SiO ₃	0.87	±0.04	Yang and Ghose, 1994
Orthopyroxene	(Mg,Fe)SiO ₃	1.28	±0.05	Chopelas, 2000
Orthopyroxene	(Mg,Fe)SiO ₃	1.05	?	Zhao et al., 1995
Orthopyroxene	MgSiO ₃	1.3	?	Hofmeister and Mao, 2002
Clinopyroxene	Ca(MgFe)Si ₂ O ₆	1.1	±0.05	Jeanloz and Thompson, 1983
Average:		1.1		
Standard Dev.		0.15		

Table 3: Enstatite Cp(av) Values Calculated from Relative Enthalpies¹

Exptl.	T ₂	H _{T₂} -H _{T₁} ²	T ₁	ΔT=(T ₂ -T ₁)	T(av) ³	Cp(av) ⁴	Cp(av)/n ⁵
Run	(K)	kJ/mol	(K)	(K)	(K)	Jmol ⁻¹ T ⁻¹	Jmol ⁻¹ T ⁻¹
Orthoenstatite							
	273.15	0.0					
EE12-B	415.6	12.64	273.15	142.45	344.38	88.73	17.75
EE1-B	513.7	22.87	415.6	98.1	464.65	104.28	20.86
EE11-B	514.1	22.73	415.6	98.5	464.85	102.44	20.49
EE4-B	638.5	36.54	514.1	124.4	576.30	111.01	22.20
EE2-B	696.6	43.3	638.5	58.1	667.55	116.35	23.27
EE20-B	724.1	46.75	638.5	85.6	681.30	119.28	23.86
EE5-B	771.7	52.16	696.6	75.1	734.15	117.98	23.60
EE13-B	849.6	61.7	771.7	77.9	810.65	122.46	24.49
EE6-B	907.9	68.89	849.6	58.3	878.75	123.33	24.67
EE8-B	968.4	76.51	907.9	60.5	938.15	125.95	25.19
EE9-B	1051.8	86.96	968.4	83.4	1010.10	125.30	25.06
EE10-B	1168.6	101.85	1051.8	116.8	1110.20	127.48	25.50
EE17	1225.4	109.51	1051.8	173.6	1138.60	129.90	25.98
Proto-enstatite							
EX17	1366	129.17					
EX11	1427	136.84	1366	61	1396.70	126.15	25.23
EX4	1481	143.47	1366	115	1423.65	124.67	24.93
EX2	1575	155.98	1481	94	1527.80	133.65	26.73
EX3	1683	169.66	1575	109	1628.85	126.08	25.22
EX26	1740	177.16	1683	57	1711.50	132.04	26.41
EX16	1745	177.83	1683	62	1714.00	132.20	26.44
EX5	1773	182.56	1683	90	1728.15	143.17	28.63
EX15	1787	184.77	1745	47	1763.60	160.55	32.11
EX10	1811	191.86	1745	67	1778.15	210.98	42.20

1 Relative enthalpies (heat content) are from Thieblot et al. (1999)

2 Values may have large errors where ΔT values are less than 70 K.

3 $\Delta H = (H_{T_2} - H_{T_1})$; $\Delta T = (T_2 - T_1)$; $T(av) = (T_2 + T_1)/2$

4 $Cp(av) = (H_{T_2} - H_{T_1}) / (T_2 - T_1) = \Delta H / \Delta T$. Cp(av) is plotted at T(av).

5 Cp/n = Cp normalized to 'n', the number of atoms in the unit formula